Strengthening of Low-Alloy Hot-Forging Steel with Nano-sized Precipitation

In a recent national research project on high-performance steels, the strengthening of medium-carbon low-alloy steel for automobile parts was extensively studied. The key technology for strengthening is the use of fine dispersions of alloy carbides several nanometers in size. Here, we describe briefly the microstructure–property relationships from our research conducted in this project.

To reduce the fuel consumption by automobiles, medium carbon steels for forging parts, such as shafts and connecting rods, must be further strengthened. When carbide-forming elements such as Ti, Nb, and V, are alloyed with carbon steels, a fine dispersion of alloy carbides and large precipitation hardening can be achieved. Continuous cooling after austenitization has been frequently reported to produce repeated nucleation of alloy carbides at ferrite/austenite interphase boundaries during the growth of ferrite or pearlite, leading to formation of precipitates in regularly spaced rows. This peculiar precipitation phenomenon is known as interphase precipitation [1].

In medium- and high-carbon steels containing vanadium, interphase precipitation of VC is used for strengthening. However, there are few studies on interphase precipitation in medium- and high-carbon steels, and the precipitates formed through interphase precipitation in those steels have not been characterized quantitatively. In this study [2],
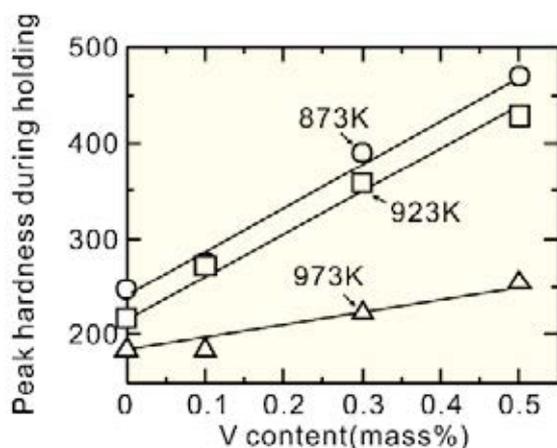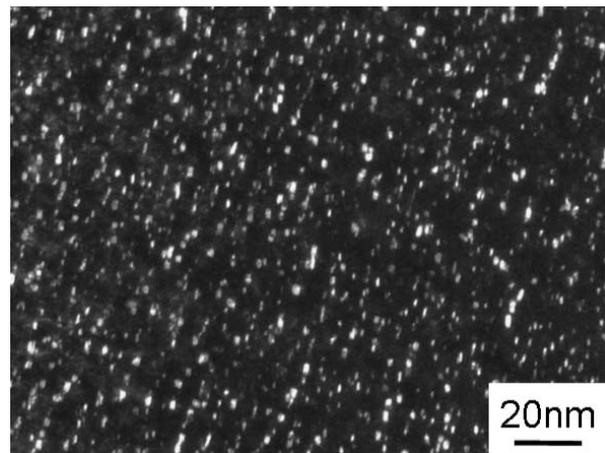

Fig. 2 Dark-field TEM of VC dispersion formed via interphase precipitation in low alloy 0.4% C steels containing 0.5% V (transformed at 923 K).

the variations in hardness and microstructure, including the size and number density of VC with V addition, have been investigated.

Fig. 1 shows the variations in peak hardness at various temperatures as a function of V content. Peak hardness increases linearly with V content at all three temperatures, while the slope at 973 K is smaller than those at 873 K and 923 K. As the temperature at which the ferrite/pearlite transformation occurs decreases, greater hardening is observed. Fig. 2 is a dark-field TEM micrograph of the interphase precipitation of VC in the 0.4% C alloy containing 0.5% V. It is clearly seen that fine VC particles (imaged as bright particles) is aligned in rows parallel to the interphase boundary. Such VC precipitation was also observed in low-alloy eutectoid steel containing vanadium.

Precipitation/dispersion strengthening can be classified into the following two categories: a cutting mechanism and a by-pass (Orowan) mechanism. A larger particle size leads to higher strength in the former case and vice-versa in the latter case. The

Fig. 1 Effects of V content on the maximum hardness of the specimens isothermally transformed at various temperatures.
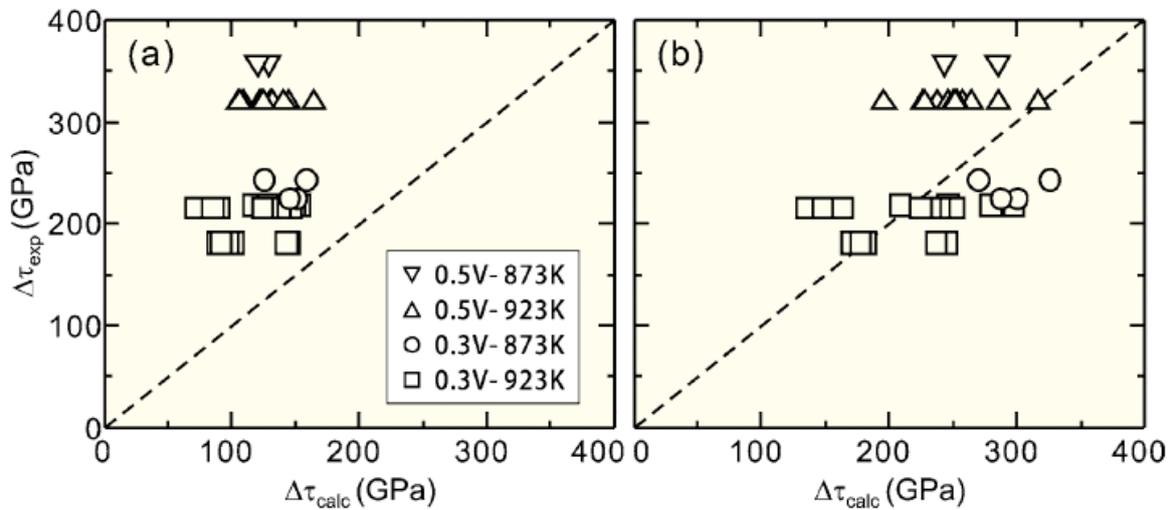
Fig. 3 Comparison of the increase in strength by precipitates between calculation based on the Ashby–Orowan model and experiments: (a) original Ashby–Orowan model where λ = x and (b) modified Ashby–Orowan model assuming λ to be 3x.

increase in yield strength in low-carbon ferritic steel containing fine alloy carbide particles is well explained by the Orowan-type dispersion hardening model modified by Ashby [3].

$$\Delta\tau_{calc} = 0.84\left(\frac{1.2Gb}{2\pi L}\right)\ln\left(\frac{\lambda}{2b}\right)$$

Here, L is the average spacing between particles in the slip plane, G is the shear modulus, b is the magnitude of Burgers vector, and λ is the outer cut-off distance.

Fig. 3 shows the relationship between the estimated and observed values. The original Ashby–Orowan model underestimates the strength significantly, as shown in Fig. 3(a). After some modification of the cut-off distance, a more reasonable agreement between observation and estimation was obtained (Fig. 3(b)). These findings were used in the first systematic, physically based model proposed to predict the microstructure and yield strength of vanadium-microalloyed medium-carbon steels [4].

References

[1] R. W. K. Honeycombe: Phase transformation in ferrous alloy, TMS-AIME, Pennsylvania, 259 (1984).

[2] G. Miyamoto, R. Hori, B. Poorganji, T. Furuhara: ISIJ Int., **51**, 1733 (2011).

[3] T. Gladman: The Physical Metallurgy of Microalloyed Steels, Maney Publishing, London p. 53 (2002).

[4] H. -H. Kuo, M. Umemoto, K. Sugita, G. Miyamoto, T. Furuhara: ISIJ Int., **53**, 669 (2012).

Keywords: steel, phase transformation
Goro Miyamoto (Microstructure Design of Structural Metallic Materials Division)
E-mail: st-mat@imr.tohoku.ac.jp
URL: http://www.st-mat.imr.tohoku.ac.jp/F-top-E.html

Structural Analysis of Amorphous Zr₅₀Ni₅₀

The structure of $Zr_{50}Ni_{50}$ amorphous alloy was analyzed by anomalous X-ray scattering (AXS) coupled with reverse Monte-Carlo (RMC) simulation. Topological features in the nearest-neighbor region suggest that the strong chemical interaction between Ni and Zr pairs breaks the icosahedral-like local ordering units commonly realized in the dense random packing of hard sphere (DRPHS) model [1].

Zr-based amorphous alloys have attracted many researchers' interests because of their characteristic physico-chemical properties [2-3]. Among them, Zr–Cu and Zr–Ni amorphous alloys have been extensively studied to elucidate the relationship between thermal stability and atomic scale structure. In the case of Zr–Ni amorphous alloy, the short distance of the Zr–Ni pair in the nearest-neighbor region was demonstrated to be a consequence of a strong chemical interaction, and this suggests crystal-like chemical short-range ordering (CSRO) around Ni [4]. Nevertheless, the available structural information is insufficient to examine and clarify the possible CSRO around Ni. This prompted us to perform AXS-RMC analysis of the Zr–Ni amorphous alloy sample. AXS-RMC analysis is suggested to be one of the most powerful methods for elucidating stereoscopic atomic configurations.

The detailed procedure of AXS-RMC analysis has been discussed previously [5,6]. For the convenience of discussion, only the important points are given below. AXS measurements at the Ni K absorption edge and the Zr K absorption edge were carried out at beam line stations 7C and NW10A of the Institute of Materials Structure Science, High Energy Accelerator Research Organization, Tsukuba, Japan. Pairs of incident energies corresponding to 25 eV and 300 eV below each of the Ni and Zr K absorption edges were employed in the present AXS measurements. The RMC modeling started with an initial model of 2,000 atoms (Zr: 1,000 and Ni: 1,000) with a body-centered cubic (BCC) arrangement in a cubic hyper-cell (density = 7.36 Mg/m³).

Fig. 1 shows the ordinary RDF measured at $E =$ 17.699 keV ($Zr\ K$ edge - 300 eV) and the environmental RDFs around Ni and Zr obtained by AXS measurements. The vertical dashed lines indicate the distances for the Ni–Ni, Ni–Zr, and Zr–Zr pairs estimated from Goldschmidt radii. The ordinary RDF suggests three kinds of correlations in the 0.2–0.4 nm range. The hump at around 0.27 nm is a harmony of the Ni–Ni and Zr–Ni pairs, and the remaining peak at 0.32 nm corresponds to the Zr–Zr pair. On

the other hand, the environmental RDF around Ni showed only the harmony of the Ni–Ni and Zr–Ni pairs; the Zr–Zr correlation in the ordinary RDF was not observed here. A similar discussion is possible for the case of AXS analysis for Zr, where the structural information on the Zr–Ni and Zr–Zr pairs is included. It should be noted that the first-neighbor Zr–Ni correlation in the ordinary RDF is obviously shorter than that for the Zr–Zr correlation. This feature could be considered as an indication of the strong chemical interaction between Zr and Ni.
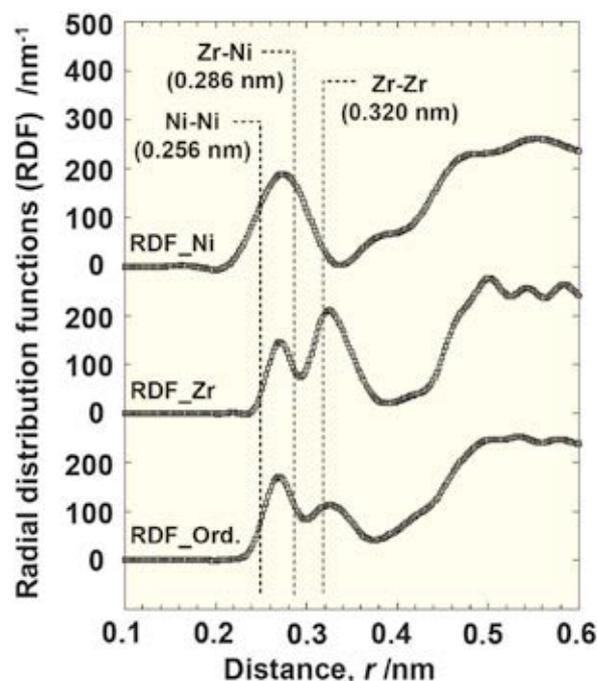

Fig. 1 Ordinary and environmental RDFs for $Zr_{50}Ni_{50}$ amorphous alloy. Vertical dashed lines indicate atomic distances estimated from the Goldschmidt radii.

The AXS-RMC analysis reproduces three independent interference functions $Q\Delta i_{Ni}(Q)$, $Q\Delta i_{Zr}(Q)$, and $Qi(Q)$, and we can discuss the three $g_{ij}(r)$ functions for $Zr_{50}Ni_{50}$ amorphous alloy, as shown in Fig. 2. Nevertheless, it should be noted that the partial structure factors and corresponding $g_{ij}(r)$ functions estimated from AXS-RMC analysis are necessary conditions at best, not sufficient conditions. The maximum peak positions for Ni–Ni

and Zr–Zr like-atom pairs indicate almost equal distance, respectively, in comparison with those estimated by Goldschmidt radii. On the other hand, the distance of the unlike-atom Ni–Zr pair is shorter than the estimated value. This feature again suggests the strong bonding between the unlike atomic pair. The calculated coordination numbers in the nearest-neighbor region indicate no strong preference for the correlation of unlike-atom pairs, as suggested in the previous report.
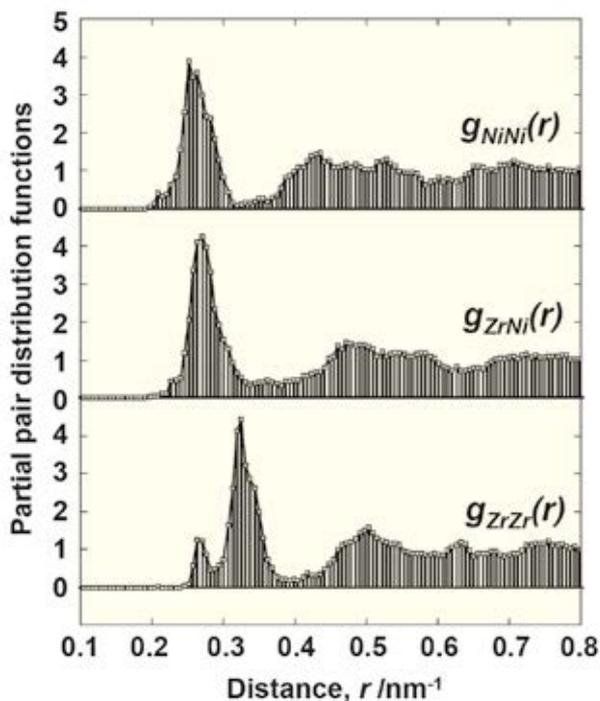

Fig. 2 Three partial $g_{ij}(r)$ functions of $Zr_{50}Ni_{50}$ amorphous alloy.

Fig. 3 shows the preferred Voronoi index around Ni found in $Zr_{50}Ni_{50}$ amorphous alloy. The ideal icosahedron with a Voronoi index (0 0 12 0 0) was found as one of the typical environments around Ni, with a 4.1 % rate of occurrence. This fraction is much larger than that around Zr (0.3 %). This result is readily explained by considering the atomic size ratio R^*: the value of R^* for Ni was much closer to that for an ideal icosahedron ($R^* = 0.90$) than that of Zr. It may be worthwhile to note that, in Zr–Ni alloys, the fraction of icosahedral structure around Ni is much smaller than that around Cu, although R^*
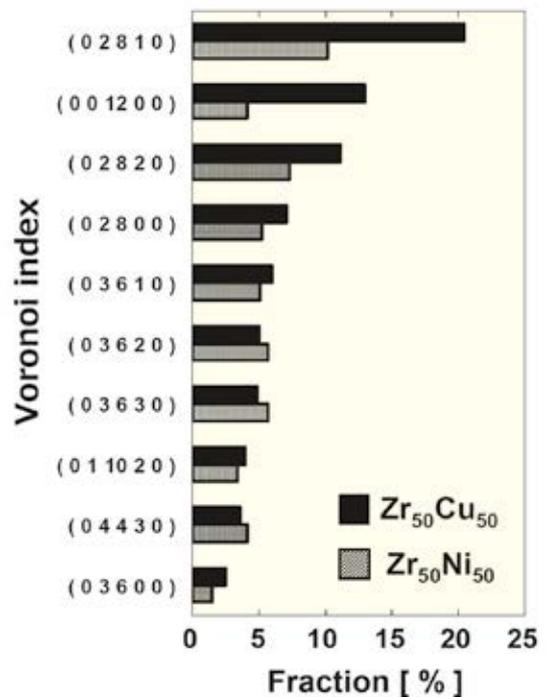

Fig. 3 Preferred Voronoi indices around Ni and Cu found in amorphous alloys. Filled and hatched bars correspond to those for $Zr_{50}Cu_{50}$ [5] and $Zr_{50}Ni_{50}$, respectively.

values for Cu and Ni show no significant difference [5]. This suggests that the strong chemical interaction between Zr and Ni breaks the icosahedral-like local ordering structure common in the DRPHS model.

References

[1] T.Kawamata, K.Sugiyama and Y.Yokoyama: Key Eng. Mater. **508**, 146–151 (2012).

[2] W. H. Wang, C. Dong and C. H. Shek: Mater. Sci. Eng. R **44**, 45–89 (2004).

[3] A. Inoue and A. Takeuchi: Mater. Sci. Eng. A **375–377**, 16–30 (2004).

[4] X. J. Liu, X. D. Hui, G. L. Chen and T. Liu: Phys. Lett. A **373**, 2488–2493 (2009).

[5] T. Kawamata, Y. Yokoyama, M. Saito, K. Sugiyama and Y. Waseda: Mater. Trans. **51**, 1796–1801 (2010).

[6] K. Sugiyama, T. Muto, T. Kawamata, Y. Yokoyama and Y. Waseda: Phil. Mag. **91**, 2962–2970 (2011).

Characteristics of Biomedical β-type Titanium Alloy Subjected to High-Pressure Torsion

β-type titanium alloy, T–29Nb–13Ta–4.6Zr (TNTZ), developed for use in biomedical applications, exhibits non-toxicity and a low Young's modulus similar to that of bone. Severe plastic deformation, such as high-pressure torsion (HPT), is effective for grain refinement and dislocation strengthening. In this study, the effect of HPT on the microstructure and hardness of TNTZ was systematically investigated to improve its mechanical strength while maintaining the low Young's modulus. In the cross sections of TNTZ subjected to HPT, a heterogeneous microstructure consisting of a matrix and an unetched band not corroded by an etching solution were observed. Both the matrix and the unetched band comprise a single β phase. Furthermore, submicron-sized grains or subgrains were formed by HPT, and grain misorientation increased with the number of HPT rotations. The hardness distribution in the cross section of TNTZ subjected to HPT was also heterogeneous; the hardness was higher in the matrix than in the unetched band when the number of HPT rotations was small. However, with increasing number of HPT rotations, the hardness of the unetched band became comparable to that of the matrix.

Stress transfer between a metallic implant and bone is non-homogeneous when the Young's modulus of the metallic implant and that of the bone are different. The Young's moduli of the metals and alloys used for fabricating metallic implants are much higher than that of bone; therefore, stress stimulation to the bone is reduced (stress shielding effect), with the result of inducing bone atrophy and then loosening of the metallic implant and re-fracturing of the bone. Thus, to mitigate the stress shielding effect, metals and alloys with Young's moduli equal to that of bone (10–30 GPa) are believed to be ideal for fabricating metallic implants [1]. Consequently, extensive efforts have been made to develop β-type titanium alloys with Young's moduli nearly equal to that of bone. One such alloy, Ti–29Nb–13Ta–4.6Zr (TNTZ), has been developed by the authors [2]. This alloy has a low Young's modulus of around 60 GPa under a solutionized condition. However, the mechanical strength of this alloy under the solutionized condition is less than that of the conventional titanium alloy, Ti–6Al–4V ELI, used for fabricating metallic implants. Thus, various thermomechanical treatments have been examined to improve the mechanical strength of TNTZ [3]. These treatments improve the mechanical strength, but they also increase the Young's modulus because a large amount of precipitates is formed. Therefore, a method that affords TNTZ with both low Young's modulus and high mechanical strength is required.

Grain refinement is generally an effective method for strengthening metals and alloys. As a method for obtaining submicron-sized grains, severe plastic deformation has attracted considerable attention. In comparison with other strengthening methods, grain refinement is expected to achieve high mechanical strength while maintaining a low Young's modulus for TNTZ because it retains the β phase, which ensures the desired low Young's modulus. Therefore, by employing high-pressure torsion (HPT) as a representative severe plastic deformation technique, we recently attempted to improve the mechanical strength of TNTZ while keeping its Young's modulus low [4, 5].

A hot-forged bar of TNTZ was used in this study. The bar was subjected to solution treatment, cold rolling, and high-pressure torsion under an applied pressure of around 1.25 GPa with a rotation speed of 0.2 rpm for 1, 5, 10, or 20 rotations (N) at room temperature. The microstructures were evaluated by optical microscopy, transmission electron microscopy (TEM), and X-ray diffraction (XRD). The hardness was measured by subjecting the specimens to the Vickers hardness test.

Fig. 1 shows optical micrographs of the TNTZ cross section subjected to HPT at $N = 10$, as a representative result. The white band (unetched band), which was not corroded by the etching solution, is observed horizontally in the middle of this TNTZ cross section. The unetched band is expected to have higher corrosion resistance than
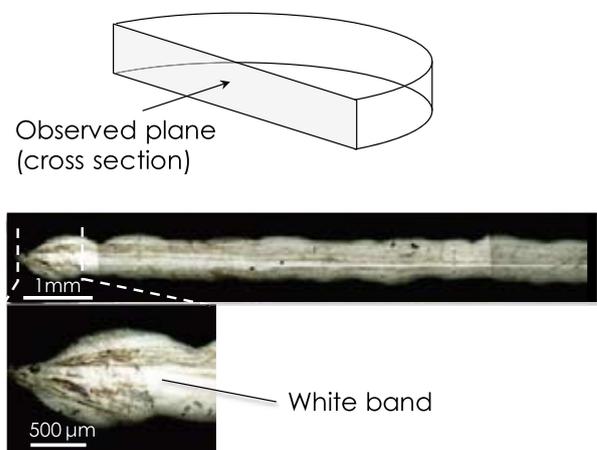

Fig. 1 Optical micrographs of cross section of TNTZ subjected to HPT at $N = 10$.
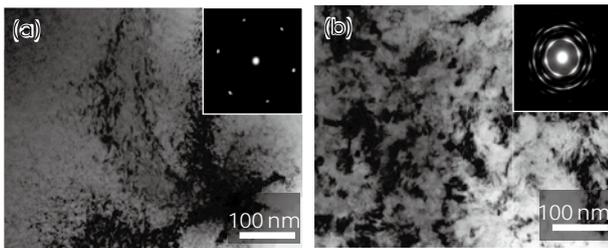
Fig. 2 Results of TEM observation at a plan view from the center of the thickness direction of TNTZ subjected to (a) cold rolling and (b) subsequent HPT at $N = 5$.

Fig. 3 Hardness distributions on cross sections of TNTZ subjected to HPT at $N =$ (a) 1 and (b) 20.

the other regions (matrix). Such unetched bands were observed in the other TNTZ cross sections subjected to HPT under all specified rotations, but they did not form after cold rolling. Furthermore, the thickness of the unetched band increased with the number of rotations and the center-to-edge distance. The equivalent strain increased with the number of rotations and the radius of the specimen. Therefore, this result indicates that the unetched band was formed in the region where a large strain was imposed.

The XRD profiles of the TNTZ surfaces subjected to cold rolling and subsequent HPT at each rotation showed only the β phase for every TNTZ specimen; the matrix in TNTZ subjected to HPT for any number of rotations is probably composed of a single β phase.

Fig. 2 shows the TEM results obtained from a plan view from the center of the thickness direction TNTZ subjected to cold rolling and subsequent HPT at $N = 5$. These regions correspond to the unetched bands observed in the TNTZ cross sections subjected to HPT. In the selected area electron diffraction patterns, spots derived from the β phase are observed in TNTZ subjected to cold rolling, whereas Debye rings appear for TNTZ subjected to HPT at $N = 5$. This result indicates that the unetched band comprises a single β phase as well as the matrix. Furthermore, small grains or subgrains are formed by HPT, and grain misorientation increases with the number of HPT rotations. In other words, the number of high-angle grain or subgrain boundaries increases with strain.

Fig. 3 shows the hardness distributions in cross sections of TNTZ subjected to HPT at $N = 1$ and 20. Overall, the hardness values tend to increase with the number of rotations. Furthermore, the hardness
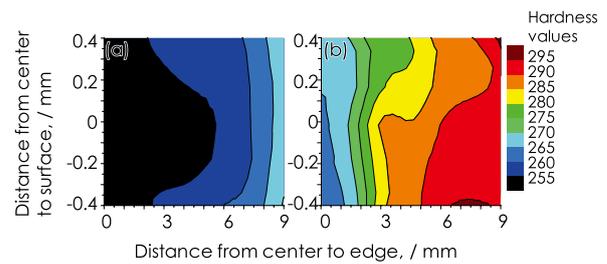
values increase gradually with the center-to-edge distance. These results indicate that the hardness increases with the equivalent strain. However, the hardness at the center of the TNTZ cross section subjected to HPT at $N = 1$ is lower than that near its surface, whereas the hardness of the TNTZ specimen subjected to HPT at $N = 20$ is almost uniform throughout the thickness direction. Unetched bands were formed by HPT at the middle of the cross sections of every TNTZ. Therefore, the hardness of the unetched band is found to be less than that of the matrix in TNTZ subjected to HPT at $N = 1$ but comparable to that of the matrix in TNTZ subjected to HPT at $N = 20$. The misorientation of grains or subgrains in the unetched band increased with the number of rotations, as shown in Fig. 2. Thus, it is considered that the hardness increases with the number of high-angle grain or subgrain boundaries.

References

[1] M. Niinomi, J. Mech. Behav. Biomed. Mater. **1**, 30 (2008).

[2] D. Kuroda, M. Niinomi, M. Morinaga, Y. Kato and T. Yashiro, Mater. Sci. Eng. A **243**, 244 (1998).

[3] T. Akahori, M. Niinomi, H. Fukui, M. Ogawa and H. Toda, Mater. Sci. Eng. C **25**, 248 (2005).

[4] H. Yilmazer, M. Niinomi, M. Nakai, J. Hieda, Y. Todaka, T. Akahori and T. Miyazaki, J. Mech. Behav. Biomed. Mater. **10**, 235 (2012).

[5] H. Yilmazer, M. Niinomi, M. Nakai, J. Hieda, T. Akahori and Y. Todaka, Key Eng. Mater. **508**, 152 (2012).

Keywords: biomedical, alloy, microstructure
Mitsuo Niinomi (Bio-Materials Science Division)
E-mail: niinomi@imr.tohoku.ac.jp
URL: http://biomat.imr.tohoku.ac.jp/

Transparent Lutetium-based Oxides Prepared by Spark Plasma Sintering

Transparent polycrystalline ceramics are promising optical materials exhibiting excellent properties that surpass single crystals. Spark plasma sintering is a versatile technique to obtain fully dense ceramics with fine grains and high transparency because of its fast densification. We demonstrated the preparations of transparent, practical, and novel Lu-based oxides by spark plasma sintering.

Rapid progress in the development of optical devices, such as lasers and scintillators, requires novel materials and processing techniques. Optical materials are commonly used in a single crystal form grown from melt. Therefore, a high melting point of a potential compound often prevents a new optical material design.

Lutetium (Lu)-based oxides, Lu_2O_3 and $Lu_3Al_5O_{12}$ (LuAG), have recently attracted much attention for their potential applications in lasers, scintillators, and phosphors because of lutetium's small ionic radius and high atomic number ($Z = 71$) among rare earth elements. Conversely, Lu-based complex oxides, such as $Lu_2Ti_2O_7$ and Lu_3NbO_7, have rarely been studied in either single crystal or polycrystalline form, due to their high melting points (over 2300 K).

Transparent polycrystalline ceramics are an alternative to single crystals because of their short production time, feasibility to produce large and complicated shapes, and high-concentration, uniform doping of active ions. The main issue in conventional sintering techniques is the requirement of homemade nanopowders. Moveover, the high temperature and prolonged time causes grain coarsening, which results in low transmittance and low mechanical properties.

Spark plasma sintering (SPS) is a versatile technique to prepare transparent polycrystalline ceramics because of its fast densification by the combination of pulsed current and uniaxial pressure (Fig. 1a). A short holding time (several minutes) and a low sintering temperature prevent grain coarsening and favor the fabrication of fine-grained ceramics with high transparencies.

Lutetium sesquioxide: Lu_2O_3

Lu_2O_3 exhibits high thermal conductivity among rare-earth sesquioxides, which makes it a promising optical medium for high power lasers. We proposed a two-step pressure sintering combined with a low heating rate to prepare transparent Lu_2O_3 ceramics (Fig. 1b) [1–3]. The preload pressure affected the intermediate relative density, and the transmittance in the visible range was more sensitive to preload pressure than that in the infrared range. A high heating rate resulted in a significant increase in density but a large grain size and porosity, which degraded transparency. The combination of a low heating rate and the two-step pressure profile resulted in a high transparency by inhibiting defect formation and eliminating pores. High transmittances
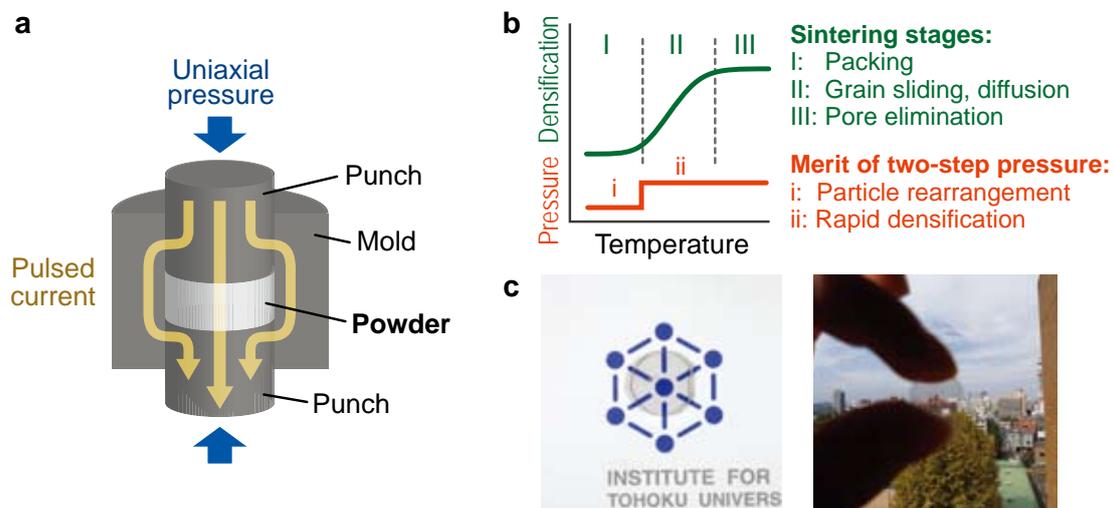

a: Uniaxial pressure — Punch — Mold — Powder — Pulsed current — Punch

b: Pressure / Densification vs Temperature
I II III

Sintering stages:
I: Packing
II: Grain sliding, diffusion
III: Pore elimination

Merit of two-step pressure:
i: Particle rearrangement
ii: Rapid densification

c: INSTITUTE FOR TOHOKU UNIVERS

Fig. 1 **a**: SPS apparatus. **b:** Densification curve and sintering stages plotted against temperature: (stage I) particle packing, (II) grain sliding and grain boundary diffusion (III) pore elimination and grain creep. The advantages of a two-step pressure profile are enhancement of particle rearrangement by a low pressure at stage I and rapid densification under a high pressure at stages II and III. **c:** Transparent Lu_2O_3 ceramic 10 mm in diameter prepared by SPS.

of 60% at 550 nm and 79% at 2000 nm were obtained under a preload pressure of 30 MPa at a heating rate of 0.17 K s^{-1} (Fig. 1c). Transparent Y_2O_3 ceramics can also be prepared by SPS using a moderate temperature and pressure profile [4].

Lutetium aluminum garnet: $Lu_3Al_5O_{12}$

Lutetium aluminum garnet ($Lu_3Al_5O_{12}$, LuAG) is a promising host medium for scintillation materials owing to its high density (6.7 Mg m^{-3}) and high effective atomic number (Z_{eff} = 63). LuAG can be an efficient and fast-response scintillator when doped with rare-earth ions such as Ce^{3+} and Pr^{3+}. Single-phase LuAG bodies with high densities (>99.5%) were obtained at sintering temperatures of 1573–1923 K. The average grain size of the LuAG bodies was 0.18–0.52 μm at 1573–1773 K and the optimal sintering temperature was 1773 K, which showed a transmittance of 77.8% at 2000 nm after annealing at 1423 K in air for 43.2 ks (Fig. 2a). Grain growth became significant at 1823 K and pores were observed at the triple junctions of the grain boundaries at high sintering temperatures, which decreased transparency [5].

Lutetium fluorite-related oxides: $Lu_2Ti_2O_7$, $Lu_2Hf_2O_7$, and Lu_3NbO_7

Lutetium titanate ($Lu_2Ti_2O_7$) has a pyrochlore structure, consisting of two interpenetrating networks of corner-sharing Ti_2O_6 octahedra and Lu_2O chains, which provides unique properties. Therefore, transparent $Lu_2Ti_2O_7$ is an interesting multifunctional material that combines optical and other properties, such as ion conduction, dielectric behavior, catalytic activity, and radiation resistance. Single-phase pyrochlore $Lu_2Ti_2O_7$ ceramics were prepared at sintering temperatures above 1273 K. A homogeneous microstructure was observed at 1573–1723 K, and grain coarsening occurred at 1823 K. The transmittance showed the highest values, 57% and 74% at wavelengths of 550 and 2000 nm, at a sintering temperature of 1723 K, which might be related to the homogeneous microstructure (Fig. 2b) [6,7]. The effect of calcination of the starting powder was also investigated [8].

Lutetium niobate (Lu_3NbO_7) has a cubic defect-fluorite structure, where Lu and Nb cations randomly occupy the 4a site, and 1/8 of the 8c sites for the O anion are statistically defective. Such disordering of
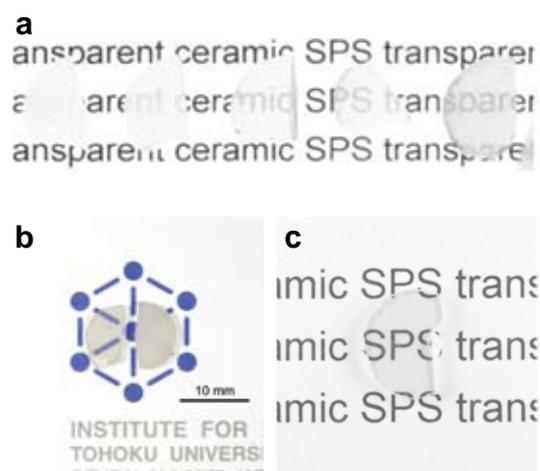

Fig. 2 **a:** Transparent LuAG ceramics sintered by SPS at various temperatures. **b:** Transparent $Lu_2Ti_2O_7$ ceramics prepared by SPS before (right) and after (left) annealing. **c:** Transparent Lu_3NbO_7 ceramics prepared by SPS (10 mm in diameter).

cations and O defects make Lu_3NbO_7 an interesting multifunctional material. We demonstrated the preparation of transparent Lu_3NbO_7 ceramics for the first time. The transparent Lu_3NbO_7 body had a uniform microstructure with an average grain size of 0.77 μm. The transmittance at 550 nm reached 68% (Fig. 2c) [9].

$Lu_2Hf_2O_7$ is a promising scintillation material, as it has the highest density (9.95 Mg m^{-3}) and high effective atomic number (Z_{eff} = 68.9) among rare-earth hafnates; however only the powder synthesis has been reported because of its high melting point (2700 K). A transparent $Lu_2Hf_2O_7$ body was prepared by reactive SPS using Lu_2O_3 and HfO_2 powders. The transmittance reached 78% at 2000 nm after annealing at 1123 K for 21.6 ks [10].

References

[1] L.Q. An, A. Ito, T. Goto, J. Am. Ceram. Soc. **94**, 695 (2011).
[2] L.Q. An, A. Ito, T. Goto, J. Eur. Ceram. Soc. **31**, 1597 (2011).
[3] L.Q. An, A. Ito, T. Goto, Ceram. Int. **37**, 2263 (2011).
[4] L.Q. An, A. Ito, T. Goto, J. Eur. Ceram. Soc. **32**, 1035 (2012).
[5] L.Q. An, A. Ito, T. Goto, J. Eur. Ceram. Soc. **32**, 3097 (2012).
[6] L.Q. An, A. Ito, T. Goto, J. Eur. Ceram. Soc. **31**, 237 (2011).
[7] L.Q. An, A. Ito, T. Goto, J. Am. Ceram. Soc. **94**, 3851 (2011).
[8] L.Q. An, A. Ito, T. Goto, Ceram. Int. **38**, 4973 (2012).
[9] L.Q. An, A. Ito, T. Goto, Mater. Lett. **65**, 3167 (2011).
[10] L.Q. An, A. Ito, T. Goto, Opt. Mater. (2012) accepted.

Keywords: ceramics, sintering, microstructure
Takashi Goto, Liqiong An, Akihiko Ito (Multi-Functional Materials Science Division)
E-mail: goto@imr.tohoku.ac.jp
URL: http://www.goto.imr.tohoku.ac.jp/

Origin of Metastability and Strain-induced Martensitic Transformation in Biomedical-grade Co–Cr–Mo Alloys with Negative Stacking Fault Energy

Biomedical-grade Co–Cr–Mo alloys are used as artificial hip or knee joints, which need significantly high wear resistance as well as good biocompatibility and mechanical properties. The phase stability of the alloys is affected by a small amount of nitrogen doping. The metastable γ-fcc phase exhibits negative stacking fault energy at room temperature. We have revealed the mechanism of meta-stability for the γ phase, which is thermodynamically stable at temperatures higher than approximately 1223 K. The strain-induced martensitic transformation has been investigated to elucidate the plastic deformation of Co–Cr–Mo alloys at room temperature.

The Co–29Cr–6Mo (CCM) alloy has two phases: a γ phase (face-centered cubic (FCC) structure) and a ε phase (hexagonal close packing (HCP) structure), which are stable at high and low temperatures, respectively. Recent research indicates that a small amount of N addition (0.1–0.16 mass%) to CCM alloy leads to the Co–Cr–Mo–N (CCMN) alloy, and full γ phase microstructure is obtained after even a moderate rate cooling from high temperature. Nevertheless, the γ phase in CCMN alloy is still metastable even at room temperature.

In our study [1], the distribution of the N atoms with respect to those of the other three elements in the alloy was observed using a 3D atom probe, as shown in Fig. 1 a, for Cr and N atoms. The N atoms (red circles) were randomly distributed about the Co and Mo, indicating that there was no obvious affinity between the N atoms and the Co or Mo atoms. However, each N atom was surrounded by Cr atoms, implying that the N atoms selectively existed in the vicinity of the Cr atoms. The density distributions of the Cr and Mo atoms are shown as functions of the distance from a N atom in Fig. 1 b. The normalized Cr atom density was markedly higher than the Mo atom density in the vicinity of the N atoms, implying that the N atoms were closer to the Cr atoms. Thus, it is apparent that the Cr atoms interact more strongly with the N atoms than do the Mo and Co atoms, which form an inert matrix in this alloy. The atomic radius of N (0.80 Å) is slightly larger than one-half of the atomic radii of Co, Cr, and Mo (1.26, 1.27, and 1.40 Å, respectively). The N dissolved in the CCMN alloy is speculated to occupy the octahedral interstitial sites of the matrix. Since an additional driving force is considered necessary to destroy or alter the existing Cr–N cluster during the γ→ε phase transformation, the γ phase is indirectly stabilized. In other words, the formation of Cr–N clusters increases the energy barrier for the γ→ε phase transition, although this transition remains a *G*-decreasing process.

On the basis of the abovementioned results, we propose a schematic model of the positioning of the elements in the CCMN alloy (Fig. 1 c). The Cr and Mo atoms are thought to be randomly distributed in
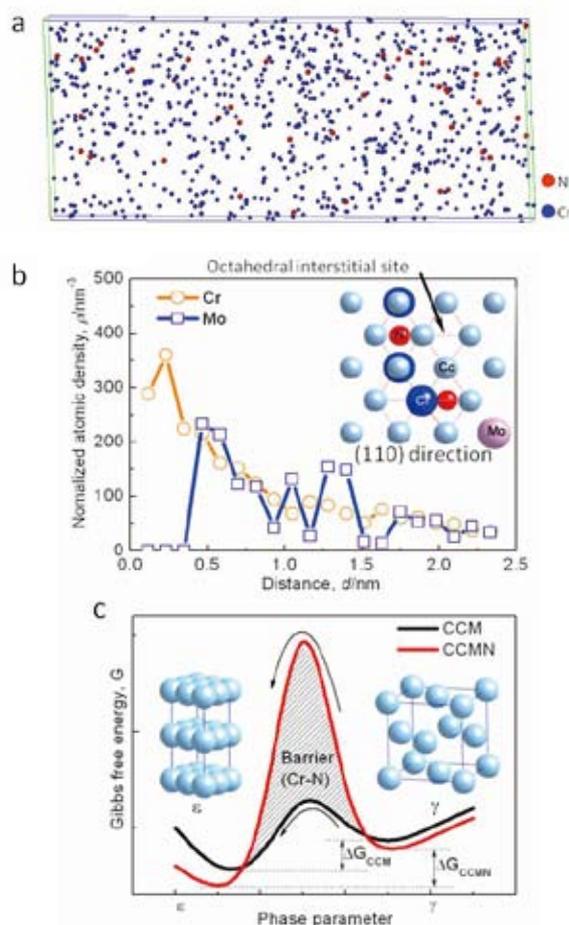

Fig. 1 (a) 3-D atom probe tomography for Cr–N. (b) Atomic density of Cr and Mo atoms as a function of distance from the N atom; the inset graph is a schematic model of the positioning of N atoms in matrix, in which N atoms selectively occupy the octahedral interstitial sites where at least one Cr atom is present in the vicinity. (c) Schematic representation of γ-phase stabilization by N addition in CCMN alloy.

the Co matrix, while the N atoms selectively occupy the octahedral interstitial sites where at least one Cr atom is present in the vicinity. In CCMN alloy, N addition accelerates the γ→ε phase transition by making *G* of the ε phase higher than that of the γ phase, but it also increases the energy barrier for

the γ→ε phase transition by the formation of Cr–N clusters. Therefore, the stability of the γ phase is controlled by these two opposite and competitive processes, and the energy barrier resulting from the Cr–N cluster formation appears to have a greater effect on the phase transition since the γ phase is effectively stabilized by N addition in CCMN alloy.

Biomedical Co–Cr–Mo (CCM) alloys have been commonly used for artificial hip and knee joint prostheses, but the need to improve their biomedical inertness and wear resistance has become widely recognized. The mechanical behaviors of CCM alloys are dominated by strain-induced martensitic transformation (SIMT), which causes crack initiation during plastic deformation but enhances the wear resistance dramatically in practical use. To develop more reliable CCM alloys, it is essential to clarify the factors affecting the occurrence of SIMT. In the present study, we investigated the effect of annealing twin boundaries (ATBs) on SIMT behavior.

We analyzed in detail the substructures near a parallel pair of ATBs after deformation under a stress that was preferential towards a slip parallel to the ATBs. Preferential formation of the ε phase at the ATBs was found by both SEM-EBSD analysis and TEM observation. A phase-field simulation was conducted by utilizing our original code developed for studying Suzuki segregation [2]. HRTEM images indicated that the thickening of the ε phase does not proceed irregularly, leaving a high-density of stacking faults. In addition, the thickness of the ε phase was found to be different even at ATBs on both sides of the twin. This difference was attributed to the internal stress due to strain incompatibility at the ATBs on the basis of a residual stress analysis by the EBSD–Wilkinson method. Fig. 2 shows the result of the EBSD–Wilkinson analysis. Fig. 2 a, b, c, and e are an image quality (IQ) map, kernel average misorientation (KAM) map, phase map, and inverse pole figure (IPF) map. SIMTed ε phase is clearly observed on the upper ATB. IQ and KAM are measures of plastic strain, and their maps indicate that plastic strain is relatively high in the region immediately above the SIMTed ε-phase. Fig. 2 e shows the distribution of internal shear stress for Shockley partial dislocation slips. The thickest ε-phase plate ($d_t \sim 1.5$ μm) is formed in the region where both the external applied stress and internal stress promote the SIMT, and thinner ε plates ($d_t \sim$
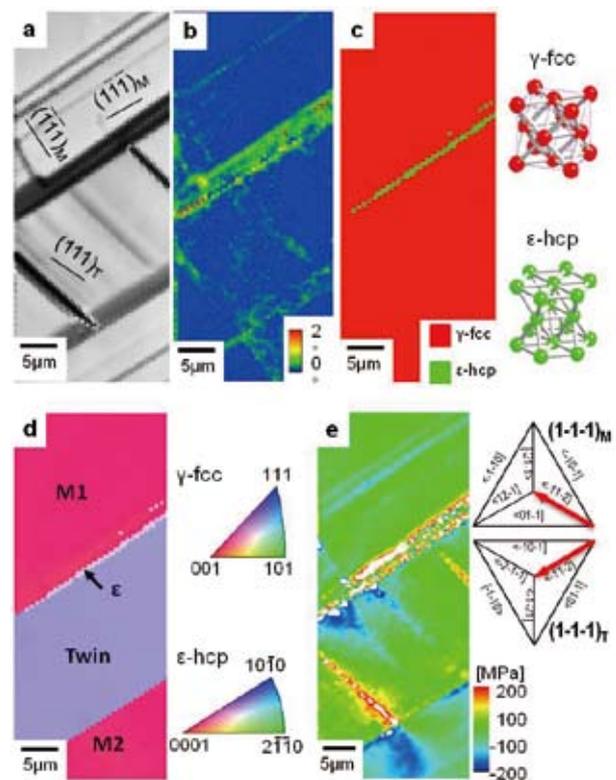

Fig. 2. SEM-EBSD micrographs of the twin-containing Co–Cr–Mo alloy. (a) Image quality (IQ) map, (b) kernel average misorientation (KAM) map, (c) phase map, (d) inverse pole figure (IPF) map, and (e) shear residual stress for (1-1-1)[-11-2]$_M$ leading partial slip.

0.5 μm) were formed in the region where the external applied stress promotes the SIMT but the internal stress suppresses it. Interestingly, very thin ε plates ($d_t < 0.1$ μm) were formed even in the region within the twin, near the boundary, despite the suppressive external stress for the SIMT and the absence of a slip trace parallel to the ATB. This is attributed to the internal stress. Thus, the effects of ATBs on SIMT have been clarified. Based on this result, more reliable biomedical CCM alloys will be developed.

References
[1] Yunping Li, Jinshan Yu, Shingo Kurosu, Yuichiro Koizumi, Hiroaki Matsumoto, Akihiko Chiba, "Role of Nitrogen Addition in Stabilizing the γ Phase of Co-29Cr-6Mo Alloy", Materials Chemistry and Physics **133**, 29 (2012)

[2] Y. Koizumi, T. Nukaya, S. Suzuki, S. Kurosu, Y.P. Li, H. Matsumoto, K. Sato, Y. Tanaka and A. Chiba, *Acta Materialia* **60**, 2901 (2012).

Development of Ni-free Ti-based Metallic Glasses and Composites with Potential for Biomedical Applications

The effects of minor additions on the glass-forming ability (GFA), thermal stability, and mechanical and corrosion properties of Ni-free Ti-based (Ti-Zr-Cu-Pd) metallic glasses were investigated. The substitution of Cu by 2% Sn significantly improved the GFA. Minor additions of Nb, Ta, and noble metal elements improved the plasticity and corrosion resistance. Using a spark plasma sintering process, large-size Ti-based bulk metallic glasses, composites, and porous glassy alloys having the approximate Young's modulus of bone were developed.

Ti-based bulk metallic glasses (BMGs) are promising materials for functional applications such as biomedical materials due to their high corrosion resistance, excellent mechanical properties, and good biocompatibility. Many Ti-based BMGs have been developed in the framework of the Ti–Ni–Cu and Ti–Zr–Cu–Ni alloy systems. However, these Ti-based BMGs contain Ni, Be, etc., which are not suitable for contact with the human body because of cellular toxicity, limiting their applications in medical fields. Recently, we developed Ni-free Ti–Zr–Cu–Pd BMGs with high strength and good corrosion resistance that make it possible to create novel Ti-based BMG implants [1]. However, a relatively low glass-forming ability (GFA) (with critical diameter of 7 mm) restricted the biomedical applications. A large critical diameter and excellent mechanical properties of BMGs are the fundamental requirements for these applications. Minor additions are fundamental to controlling the formation, manufacture, and properties of metallic materials by controlling nucleation during solidification. In this study, we investigated the effect of minor additions on GFA, thermal stability, and the mechanical and corrosion properties of the Ti–Zr–Cu–Pd glassy alloy system [2,3].

The substitution of Cu by 2% Sn significantly improved the GFA. A $Ti_{40}Zr_{10}Cu_{34}Pd_{14}Sn_2$ bulk glassy alloy rod with a diameter of 12 mm has been fabricated by a copper mold casting technique (Fig. 1). The addition of 2–4% Sn enlarged the supercooled liquid region, indicating good thermal stability. TiZrCuPdSn bulk glassy alloys exhibited high compressive strengths of about 2000–2050 MPa [2]. We also implanted the Ti-based ($Ti_{40}Zr_{10}Cu_{34}Pd_{14}Sn_2$) BMG bars under the skin and in the bone of rats. The Ti-based BMG bars exhibited excellent biocompatibility in both soft and hard tissue. They also showed nice osteoconductivity when implanted in bone tissue, and no metal ion diffusion was found up to one month after implantation.

High strength and distinct plastic strain were observed in the stress–strain curves for Nb-added Ti–Zr–Cu–Pd alloys. A yield strength exceeding 2050 MPa, low Young's modulus of about 80 GPa, and distinct plastic strains of 6.5% and 8.5% corresponding to serrated flow sections were obtained for the 1% (Fig. 2) and 3% Nb-added alloys, respectively. These minor additions of Nb or Ta also exhibit higher corrosion resistance, as shown in Fig. 3. The minor addition of noble metal elements (Au, Pt) can significantly improve the plastic stain of the Ti–Zr–Cu–Pd glassy alloys (Fig. 2) due to nanoparticles dispersed in the glassy matrix blocking the propagation of shear bands [3].
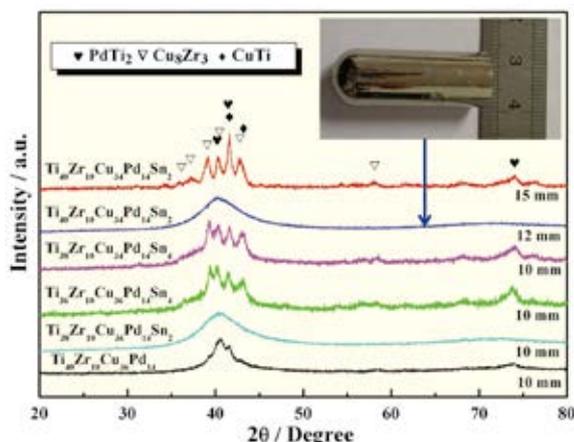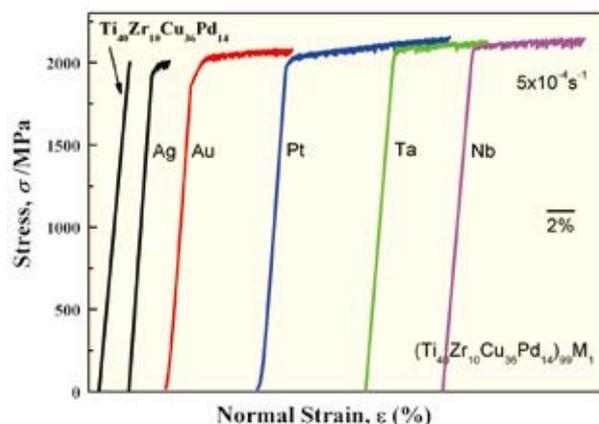

Fig. 1 XRD patterns of TiZrCuPdSn alloys.

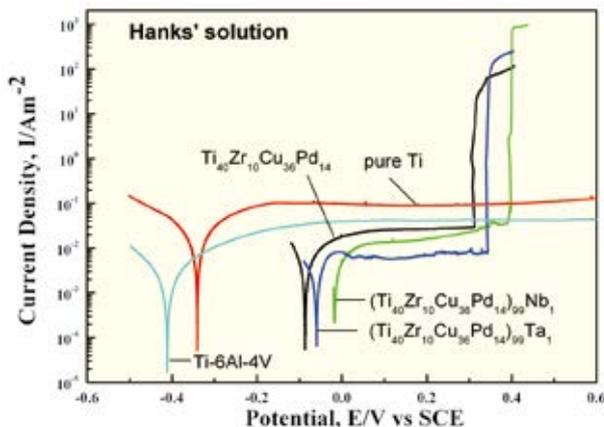Fig. 2 Compressive stress–strain curves of the $(Ti_{40}Zr_{10}Cu_{36}Pd_{14})_{99}M_1$ alloys.

Fig. 3 Potentiodynamic polarization curves of the $(Ti_{40}Zr_{10}Cu_{36}Pd_{14})_{99}M_1$ alloys at 310 K. The curves of pure Ti and Ti–6Al–4V alloy are also shown for comparison.

It is known that BMGs are commonly produced using solidification techniques such as copper mold casting or water quenching. However, when using a solidification technique, a rather high cooling rate is required to suppress the formation of more thermodynamically stable crystalline phases. The sample size and shape are seriously limited, thereby limiting the range of applications. On the other hand, by using a consolidation technique, it is possible to produce larger metallic glassy alloy parts in a greater variety of shapes than by using a solidification technique. Spark plasma sintering (SPS), developed as a rapid consolidation technique, has great potential for producing large-size glassy samples in a short sintering time [4,5].

We prepared Ti-based metallic glassy powders using a high-pressure argon gas atomization method. Using the glassy alloy powders, or their mixed powders blended with hydroxyapatite (HA) powder, we produced Ti-based BMGs and composites with diameters over 15 mm by the SPS process [6,7]. The HA particles were uniformly distributed in the glassy matrix. No crystallization of the glassy matrix was observed. The thermal stability was almost independent of the addition of the HA particles. The produced composites exhibited lower Young's moduli than those of the as-cast Ti-based bulk glassy alloys.

Furthermore, we also produced porous Ti-based BMGs (Fig. 4) with diameters over 15 mm by

spark plasma sintering a mixture of gas-atomized Ti-based glassy alloy powders and solid salt (NaCl) powders, followed by a leaching treatment into water to eliminate the salt phase. Pores were homogeneously distributed in all of the sintered samples. The porosity can be controlled by controlling the volume fraction of the added salt phase. In this way, high-strength porous Ti-based BMGs with low Young's modulus, equal to that of bone, can be obtained.
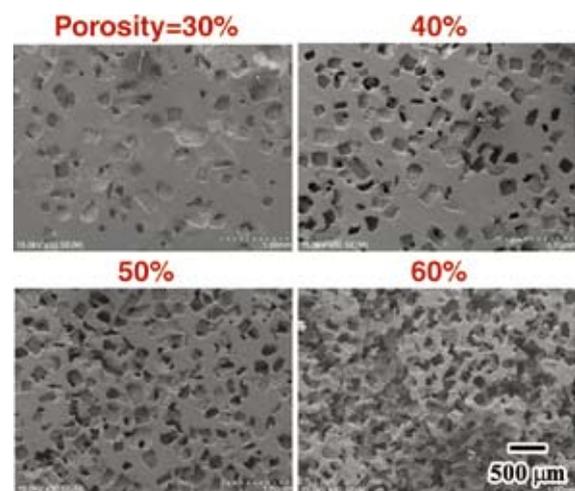

Fig. 4 SEM images of sintered porous Ti-based (TiZrCuPdSn) samples, after leaching NaCl, with various porosities produced by the spark plasma sintering process at 643 K, 600 MPa, 10 min.

References

[1] S.L. Zhu, X.M. Wang, F.X. Qin, M. Yoshimura and A. Inoue, Mater. Trans., **48**, 2445 (2007).

[2] S.L. Zhu, G.Q. Xie, F.X. Qin, X.M. Wang and A. Inoue, Mater. Trans., **53**, 500 (2012).

[3] F.X. Qin, G.Q. Xie, Z.H. Dan and A. Inoue, Applied Mechanics and Materials, **148-149**, 241 (2012).

[4] G.Q. Xie, D.V. Louzguine, H. Kimura and A. Inoue, Appl. Phys. Lett., **90**, 241902 (2007).

[5] G.Q. Xie, D.V. Louzguine, H. Kimura, A. Inoue and F. Wakai, Appl. Phys. Lett., **92**, 121907 (2008).

[6] G.Q. Xie, F.X. Qin, S.L. Zhu and A. Inoue, Intermetallics, **29**, 99 (2012).

[7] S.L. Zhu, X.J. Yang and Z.D. Cui, Intermetallics, **19**, 572 (2011).